# Multi-Dimensional Widefield Infrared-encoded Spontaneous Emission Microscopy: Distinguishing Chromophores by Ultrashort Infrared Pulses

Chang Yan*[1], Jackson C. Wagner[1], Chenglai Wang[1], Jianyu Ren[1], Carlynda Lee[1], Yuhao Wan[2], Shizhen E. Wang[2], and Wei Xiong*[1,3,4]

[1]Department of Chemistry and Biochemistry, University of California San Diego, La Jolla, California 92093, United States

[2]Department of Pathology, University of California San Diego, La Jolla, California 92093, United States

[3]Materials Science and Engineering Program, University of California San Diego, La Jolla, California 92093, United States

[4]Department of Electrical and Computer Engineering, University of California San Diego, La Jolla, California 92093, United States

*Corresponding Authors:

Chang Yan: c7yan@ucsd.edu

Wei Xiong: w2xiong@ucsd.edu

**Abstract**

Photoluminescence (PL) imaging has broad applications in visualizing biological activities, detecting chemical species, and characterizing materials. However, it is often limited by the total number of independently resolvable chromophores within the detection spectral windows, constraining the information encoded in an image. Here, we report a PL microscopy based on the nonlinear interactions between mid-infrared and visible excitations on matters, which we termed Multi-Dimensional Widefield Infrared-encoded Spontaneous Emission (MD-WISE) microscopy. MD-WISE microscopy demonstrates multiplexity in a three-dimensional space, by distinguishing chromophores that possess nearly identical emission spectra through three independent variables: the temporal delay between the infrared and the visible pulses, and the optical frequencies of the two pulses. More importantly, MD-WISE method operates at widefield imaging conditions, other than the confocal configuration adopted by most nonlinear optical microscopies which require focusing the optical beams tightly to reach high intensity for nonlinear interactions. MD-WISE microscopy is enabled by two mechanisms: 1. Modulating the optical absorption cross sections of molecular dyes by exciting specific vibrational functional groups; 2. Reducing the PL quantum yield of semiconductor nanocrystals through strong field ionization of excitons. By demonstrating the capacity of registering multi-dimensional information into PL images, MD-WISE microscopy has the potential of expanding the number of species and processes that can be simultaneously tracked in high-speed widefield imaging applications.

## Introduction

Photoluminescence (PL) imaging techniques based on spontaneous emission have achieved single-molecule level sensitivity (1, 2) and sub-diffraction spatial resolution (3), becoming vital tools for fields from bioimaging (4, 5) to material characterization (6). However, an intrinsic limitation has been the number of color channels available for multiplexed imaging, since PL chromophores in the visible and adjacent spectral regions often have broad emission spectra which can easily overlap with each other (7). Thus, techniques that involve other molecular degrees of freedoms have been developed for multiplexed imaging. For instance, the narrow absorption linewidths of molecular vibrations allow more than 20 chromophores to be independently resolved using stimulated Raman microscopy (8). Vibrational chemical imaging methods based on Raman microscopy (8–10) and infrared (IR) photothermal microscopy (11) have been highly successful, but the detection limits of such methods are generally less sensitive than PL-based techniques.

Recently, a few techniques have emerged to encode vibrational information into fluorescence, a specific form of PL emission (12–18). Nonlinear optical methods, which resonantly excite multiple transitions of a molecule, have enabled encoding processes based on the inherent nonlinear optical response of dye molecules (12). Using the stimulated Raman transition to excite vibrational modes and encode a fluorophore's emission intensity, stimulated Raman excited fluorescence microscopy (15, 19) has been demonstrated as a powerful multiplexed PL imaging method with single-molecule level sensitivity at ambient conditions. However, nonlinear optical microscopies typically operate by focusing optical beams tightly onto the sample of interest, since the cross-sections of higher order nonlinear interactions are orders of magnitudes lower than first-order absorption cross-sections. This imaging condition has limited the possibility of applying nonlinear optical processes in widefield multiplexed PL imaging. Photothermal encoding methods that modulate fluorescence signal by the change of the temperature around fluorophores following vibrational relaxation have also been explored in the fluorescence-detected mid-infrared photothermal microscopy (17, 18). While photothermal methods are

very sensitive and useful, they are intrinsically based on the optical response of a fluorophore to changes in the matrix environment, making their sensitivity dependent on properties of the matrix (20, 21).

Though difficult, it is useful to develop nonlinear optical multiplexed widefield PL microscopy due to certain intrinsic advantages such as lower photodamage and faster imaging speed over a large field of view than confocal microscopy (22, 23). Widefield microscopies have been successful for tracking fast cellular dynamics (23) and fast energy dissipation processes in materials (24). Multiplexed PL images are encoded with a large amount of information which needs to be collected over a set of different imaging conditions such as excitation frequencies. As the multiplexed data collection process can be time-consuming, the widefield mode may become an important module for fast multiplexed PL imaging methods.

A general strategy of nonlinear optical multiplexed PL imaging is to excite other degrees of freedom in addition to the linear electronic transitions to modulate the electronic absorption or the subsequent PL emission process, as demonstrated in prior works of nonlinear spectroscopy (25–27). The nature of a widefield nonlinear optical microscope demands these additional optical processes to possess large cross-sections, so that they are compatible with the condition of lower photon flux. With ultrashort femtosecond mid-IR pulses, two types of processes come to the rescue, where IR excitations modulate the associated electronic absorption or emission processes (referred as IR-Visible nonlinear interactions). The first type of process is exciting molecular vibrations through the linear absorption of a mid-IR photon that further modulate the electronic absorptions. Linear mid-IR absorption typically has a much larger cross-section than nonlinear vibrational excitation such as Raman-based processes (11, 12). The infrared-visible double-resonance process (12), during which a dye molecule sequentially absorbs a mid-IR photon and then a visible photon, can encode PL signals in the widefield configuration (14, 28–30). The second IR-visible nonlinear interaction is based on the strong electric field of femtosecond mid-IR pulses, which can reach the order of megavolts per centimeter (MV/cm) due to the high peak power and the relatively long wavelength (31, 32). Such electric fields can ionize excitons in semiconductor materials, affecting the PL

intensity of quantum dot (QD) emitters (33). Herein, we synthesize both types of processes described above to demonstrate that the action of a mid-IR pulse can distinguish PL chromophores, including molecules and QDs, in multiplexed widefield imaging via the distinct responses of the chromophores either to the IR frequency or the temporal delay between ultrashort pulses.

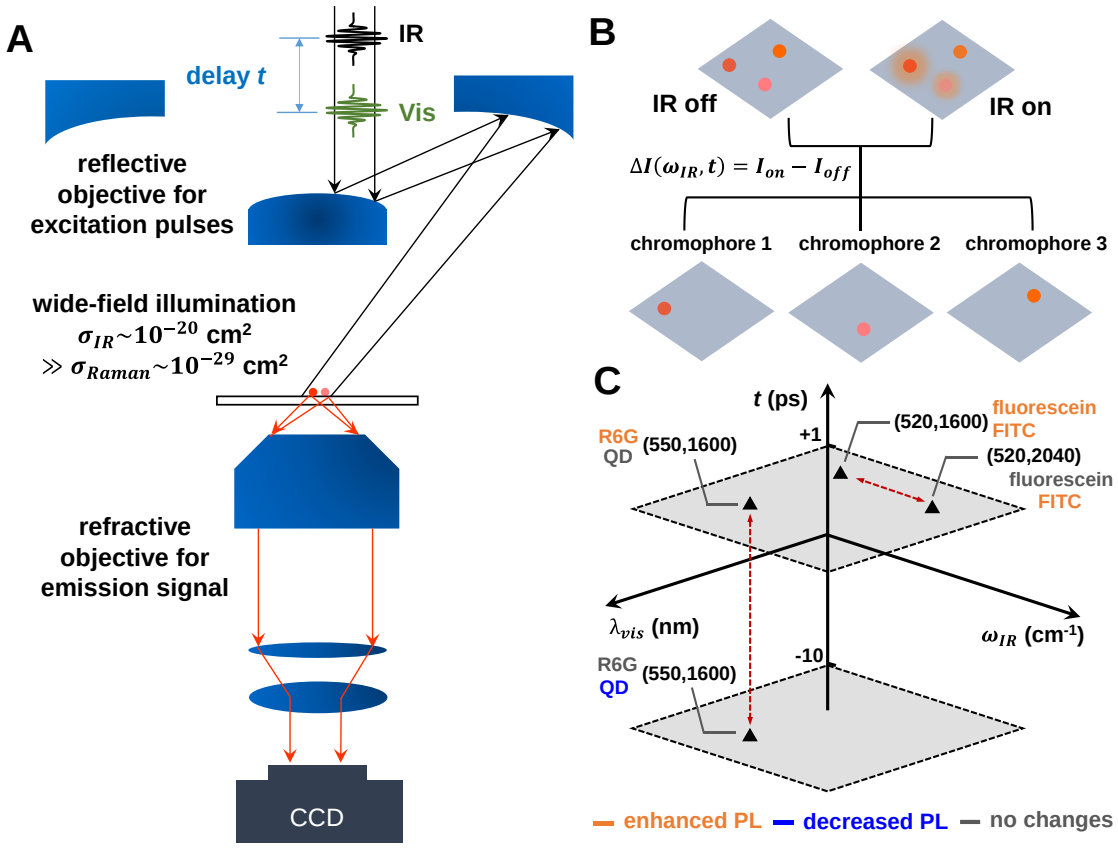


**Fig. 1 (A)** Schematic illustration for MD-WISE microscopy, positive delay of *t* denotes that the IR pulse arrives earlier than the visible pulse. **(B)** The intensity of PL signals generated following the visible excitation pulse can be encoded by the optical frequency of IR pulse or the delay *t*. By taking the difference images with or without IR pulse, various chromophores can be distinguished apart even if their emission spectra are nearly identical. **(C)** The change of a chromophore's PL induced by the IR pulse, either there is no change (gray), or increased PL (orange) or decreased PL (blue), is a function of independently tunable variables expressed as the three orthogonal axes: visible excitation wavelength $\lambda_{vis}$ (nm), IR frequency $\omega_{IR}$ (cm$^{-1}$), and ultrafast delay *t* (ps). By choosing a condition (▲) in the three-dimensional space, pairs of chromophores with nearly identical PL spectra can be distinguished from each other, such as the pairs of QD versus R6G and FITC versus fluorescein. The two gray shaded planes are condition planes having the same delay, +1 or -10 ps, and the coordinates in brackets are expressed as ($\lambda_{vis}$, $\omega_{IR}$).

**Principles of MD-WISE microscopy**

We referred this approach as the Multi-Dimensional Widefield Infrared-encoded Spontaneous Emission (MD-WISE) microscopy. The general idea, basic design and unique capability of MD-WISE microscopy is shown in Fig. 1. A pair of femtosecond IR and visible pulses delayed by a controlled interval, *t*, travel collinearly and are spatially focused onto the sample of interest by a reflective objective. The spontaneously emitted PL signals from the chromophores, following the ultrafast interactions of the two pulses, are collected by a refractive objective to form a widefield image on a conventional charge-coupled device (CCD) camera (Fig.1A). The intensity of the PL image is a function of the optical frequencies of the IR and visible pulses, as well as the temporal delay *t*. Thus, as shown in Fig. 1B, by taking the intensity difference of the PL images acquired with or without the IR pulse, we obtain difference images revealing species of which the PL is encoded by the IR pulse, either through vibrational excitation or strong field interactions, as described above.

Because the mechanisms that encode PL are time-dependent, MD-WISE realizes a three-dimensional condition space formed by the three orthogonal variables as illustrated in Fig. 1C: the IR frequency, the visible wavelength, and the ultrafast delay *t*. By choosing the appropriate condition in the space, many chromophores having nearly identical PL spectra or emitting in the same PL collection wavelength range thus can be distinguished in MD-WISE. By demonstrating the capacity of registering multi-dimensional information into widefield PL images, MD-WISE microscopy has the potential of further expanding the number of species and processes that can be simultaneously tracked in high-speed chemical and biological imaging applications.

**Results and Discussions**

***IR-encoding mechanism 1: infrared-visible double-resonance process.***

We first demonstrate one of the two mechanisms of MD-WISE microscopy: using vibrational excitation to alter the electronic absorption cross-section and the subsequent PL emission of molecular

dyes. This type of double-resonance process (12) has been previously investigated in various types of experiments that utilize mid-IR pulse to encode vibrational information into fluorescence signals (13, 14, 16, 28, 34). An eminent example is the broadband fluorescence-encoded IR spectroscopy that operate under the confocal configuration to read out the vibrational spectrum of coumarin molecules in the solution phase (16, 34–36). For widefield PL imaging, an early work, transient fluorescence detected IR microscopy, showed that one can use fluorescence signals to image the spatial distribution of generic C-H and N-H stretch modes of dyes at the IR frequency of ~3000 $cm^{-1}$ (14). Yet, the broad potential of multiplexed PL imaging has not been explored in this work. Below, we report the effect of vibrationally exciting functional groups linked to various sites of dye molecules and discuss how these diverse groups can be used to differentiate nearly identical PL chromophores in widefield imaging.

Rhodamine 6G (R6G) molecules, a prototypical fluorophore with a high fluorescence quantum yield (QY), is examined first. The solid-state linear IR absorption spectrum of R6G (Fig. 2A), shows a sharp peak at 1600 $cm^{-1}$, which is a ring stretch mode associated with the xanthene tri-ring conjugation system (marked as green), and a peak at 1720 $cm^{-1}$ assigned to the carbonyl stretch of the ester group (marked as blue) (37, 38). In the double-resonance excitation scheme here, the IR pulse first promotes a vibrational mode of R6G to the first excited state, $v = 1$ (Fig. 2B). Many vibrational modes of R6G could be involved in vibronic couplings. Due to the shift in energy levels and changes in Frank-Condon factors (35), the electronic absorption spectrum of $v = 1$ state is altered from that of $v = 0$ ground state. Therefore, the absorption cross-section of the visible photon at a specific wavelength changes. Next, before vibrational relaxation, the visible pulse excites the molecules to the $S_1$ electronically excited state. The absorption cross-section difference is read out through fluorescence, as the molecule returns to the ground state $S_0$. The QY of the fluorescence emission process is not affected by the IR excitation because the molecule, regardless of which vibronic state it is in immediately after the visible excitation, first relaxes to the lowest vibronic state in $S_1$ on an ultrafast timescale before emitting the fluorescence (39).

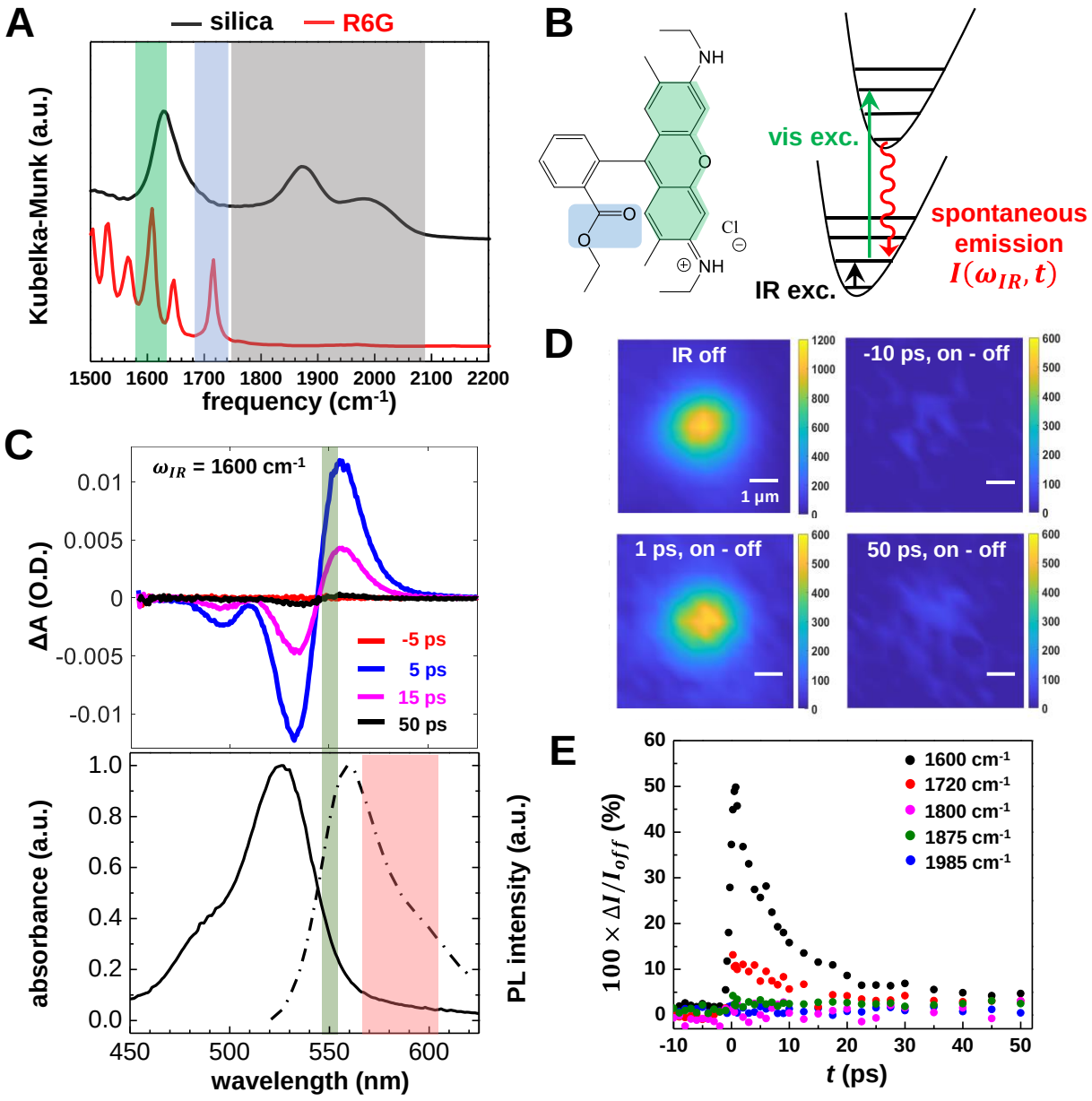


**Fig. 2 (A)** DRIFTS results of silica microspheres and pure R6G dye. The colored shade areas mark the IR excitation frequencies covered in MD-WISE imaging experiments of silica spheres stained with R6G: the aromatic three-ring xanthene system (green), the ester group (blue) and silica absorption (grey). **(B)** Molecular structure of R6G, and scheme of double-resonance excitation process and the subsequent spontaneous emission of fluorescence. **(C)** Ultrafast transient absorption (upper panel) spectra of R6G in IR-pump-Vis-probe experiments. The steady-state absorption (solid line) and emission spectra (dashed line) of R6G-stained silica beads are in the bottom panel. The green area marks the excitation wavelength of the visible pulse, tuned to the excited-state absorption region in the pump-probe spectra. The red shaded area marks the collection window of the emission signal. **(D)** Widefield images of a silica bead, including the image collected without IR excitation and several difference images collected with the 1600 ± 30 $cm^{-1}$ IR pulse delayed at different times. The colorbars represent the counts on the CCD pixels. Scale bars are 1 micron. **(E)** The kinetic traces of the relative difference of emission intensity in the widefield images acquired with and without IR pulse, measured with five different center frequencies of the IR pulse.

We verified the effect of mid-IR excitation on the electronic absorption spectrum with IR-pump-visible-probe transient absorption experiments. The upper panel of Fig. 2C displays the transient absorption spectra of R6G in dimethyl sulfoxide-$d_6$ solution measured at several delays. The IR excitation is tuned to the xanthene stretch mode at 1600 $cm^{-1}$. For short delays such as 5 or 15 ps, it is evident that there is change in the absorbance across the visible spectrum, in contrast to the signal at negative delays or long delays such as 50 ps. Thus, the effect of IR excitation is an ultrafast double-resonance effect rather than a photothermal effect. At longer visible wavelengths, the sample exhibits a positive $\Delta A$ value, indicating the visible absorption is enhanced by IR excitation; on the contrary, the visible absorbance at shorter wavelength is reduced due to the bleaching of $v = 0$ populations. Thus, when the IR excitation is on, it leads to more absorption near 550 nm, which leads to more fluorescence emission.

From the combined knowledge of transient and linear spectra (Fig. 2C), we can select a narrowband visible excitation wavelength centered at 550 ± 5 nm (green area in Fig. 2C) for MD-WISE imaging experiments. At 550 nm, there is a high $\Delta A$ to form a bright difference PL image, with sufficient low linear absorption (thus, low background PL) to achieve good signal-to-noise ratio. Furthermore, a 550 nm excitation has enough spectral shift from the PL detection window 585 ± 18 nm (red area in Fig. 2C) to eliminate leakage of excitation photons. The actual excitation and PL detection wavelengths of other dye molecules such as fluorescein could vary but are selected using the same criteria.

The next step is to examine the effect of IR excitations on widefield PL images. A set of widefield PL images of a R6G-stained microbead (diameter = 3 microns) is displayed in Fig. 2D. The set includes an image collected without IR excitation and several difference images collected with the delay $t$ set to -10 ps, 1 ps, and 50 ps, respectively, with IR excitation range at 1600 ± 30 $cm^{-1}$. The difference images are generated by subtracting the PL image without the IR pulse from the one with the IR pulse. At the short positive delay of 1 ps, the IR pulse enhances the emission signal strongly, because most of the vibrationally excited molecules have not relaxed yet. Furthermore, the difference image at 1 ps agrees with the no IR PL image, reflecting that it faithfully reproduces the shape of the microbead and the spatial

distribution of R6G. In contrast, the microbead disappears in the difference images at -10 ps and 50 ps since the molecules have returned to the vibrational ground state.

To characterize the vibrational dynamics and the IR frequency dependence of PL encoding, we measured the ultrafast kinetics of the PL intensity change for a series of IR excitation frequencies (Fig. 2E). At a specific delay *t*, the IR-induced change of PL intensity per CCD pixel, $(I_{on} - I_{off})/I_{off}$, is calculated by averaging the relative intensity change among all the CCD pixels in a 2.5 μm by 2.5 μm box that centers around the microbead. Only when the IR frequency is tuned to the vibrational modes of R6G, the PL intensity is encoded. When the IR frequency center is tuned to 1800, 1875, 1985, 2050 and 2100 $cm^{-1}$ to cover the modes of silica in the range 1800-2100 $cm^{-1}$ (the gray box in Fig. 2A), the kinetic traces in Fig. 2E show no modulation or encoding signal. This indicates that exciting the silica substrate does not change PL intensity. Thus, the IR-induced PL change originates from intramolecular processes. The extent of PL change differs among various vibrational modes of R6G. The highest occupied molecular orbital (HOMO) and lowest unoccupied molecular orbital (LUMO) of R6G are located on the xanthene ring conjugation system. Thus, it is expected that the 1600 $cm^{-1}$ vibrational mode of the xanthene has a stronger effect on the electronic absorption spectrum than the 1720 $cm^{-1}$ carbonyl stretch mode of the ester group. The carbonyl stretch mode is a relatively local mode involving mostly the displacements of ester group atoms, but it could couple with the displacements of the xanthene atoms. The unexpected result that non-xanthene groups can affect PL intensity relaxes the conditions of where vibrational tags can be installed on chromophores and expands the possible library of chromophores for MD-WISE imaging.

***IR-encoding mechanism 2: strong field ionization of excitons in QDs.***

The scope of this work is further expanded beyond molecular fluorescence to PL emission of semiconductor nanocrystals. QD chromophores, which are semiconductor nanocrystals, are bright emitters of which the PL intensity can be encoded by an ultrashort IR pulse (33). However, the second mechanism is distinct from mechanism 1 discussed above. The IR-induced PL change of QDs originates

from the strong electric field strength of an ultrashort mid-IR pulse which can drive electrons of excited-state QDs to overcome the potential barriers in core/shell QDs, leading to events such as the discharging of trion states and the dissociation of excitons (33). The low frequency phonon modes of inorganic nanocrystals are off-resonant from the IR frequencies (1600~2100 $cm^{-1}$) used in this study, and thus do not interact with the IR pulse.

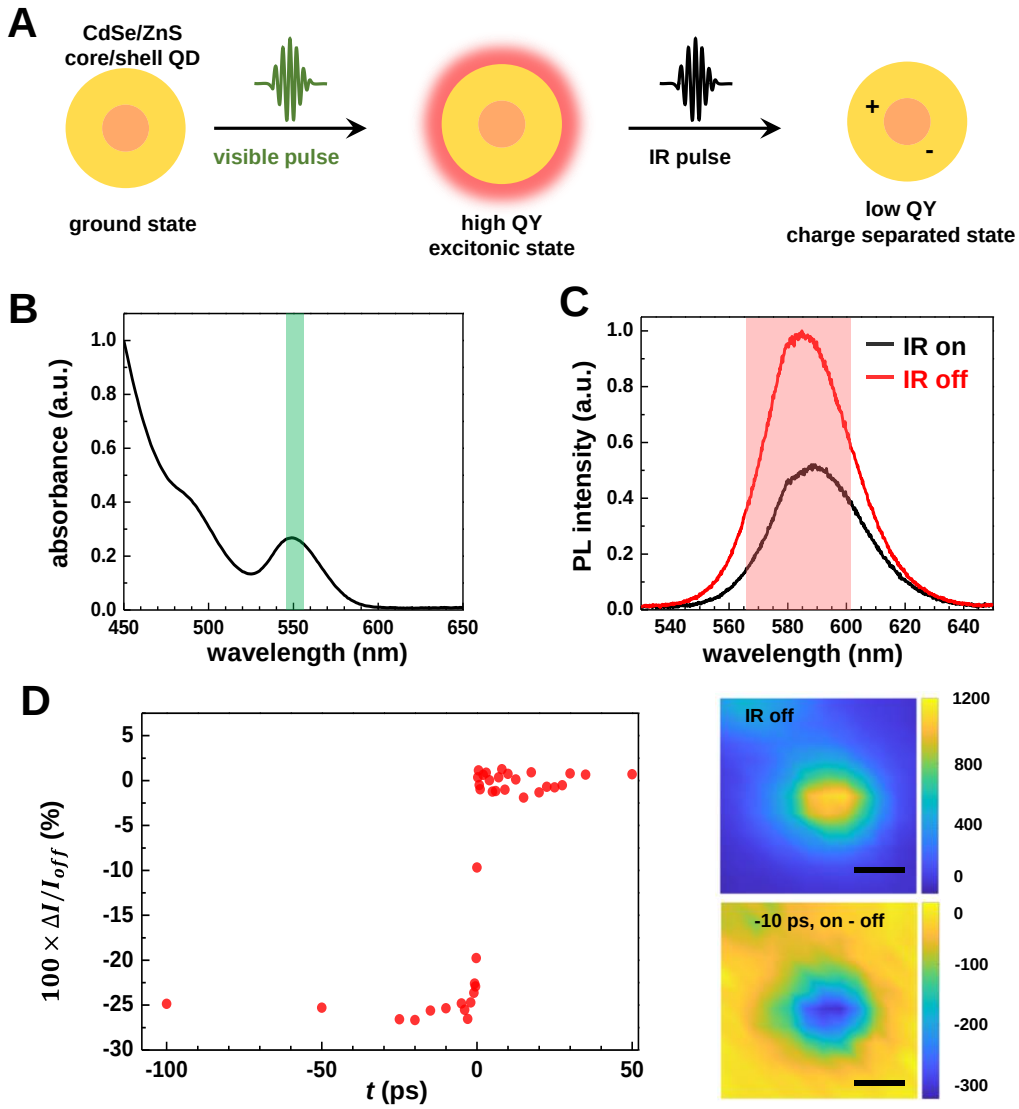


**Fig. 3 (A)** Illustration on the process during which the electric field of mid-IR pulse quenches the PL emission of a QD following visible pulse excitation. **(B)** Visible absorption spectrum of the QD-stained silica microspheres, and the visible excitation wavelength (green) in MD-WISE imaging. **(C)** PL spectra of the QD-stained silica microspheres, showing that IR pulse (2100 ± 30 $cm^{-1}$) reduces the emission intensity significantly and redshifts emission spectrum. The red area represents the collection window used for MD-WISE imaging. **(D)** The kinetic trace of the relative difference of emission intensity in the widefield images induced by the IR pulse (2100 ± 30 $cm^{-1}$). A widefield image of a silica bead without IR excitation and a difference image with the IR pulse delayed to -10 ps show that the PL signal is significantly quenched by the IR. Scale bars are 2 microns.

The encoding mechanism employed here is illustrated in Fig. 3A. First, the visible pulse excites the CdSe/ZnS core/shell QD into an excitonic state. If no IR pulse arrives, the exciton in QD would eventually emit a photon with a certain QY. If an IR pulse arrives before the emission occurs, the high electric field strength, ~50 MV/cm for the condition applied here, can dissociate the electron-hole pair of an exciton into separated charge carriers. The charge-separated state has a significantly lower QY for PL emission than the excitonic state (40, 41), and therefore the action of the IR pulse quenches the PL intensity of a QD. This strong field effect of the IR pulse on QDs shares some similarities with the strong field ionization in atomic and molecular optics where an intense long wavelength laser pulse favors ionizations in atoms and molecules through tunneling ionizations and can drive the electrons further from the ionized atoms to mitigate recombination (42, 43).

We used a 550 ± 5 nm (green area in Fig. 3B) visible pulse to excite the first-excitonic absorption feature of the CdSe/ZnS QDs, then a strong IR pulse arrives. The frequency range of IR pulse is tuned to 2100 ± 30 $cm^{-1}$, but the precise value can vary since the IR frequency is off-resonant: what matters is the electric field strength (33). In Fig. 3C, we plot the PL spectra of QD-stained silica beads acquired with and without the IR pulse. The temporal delay *t* is -100 ps. It is evident that the PL intensity drops significantly and the PL spectrum redshifts due to the formation of low QY charge separated states following the action of the IR pulse. As shown in Fig. 3D, the quenching of PL intensity measured from MD-WISE images of QD-stained silica beads starts sharply as delay *t* becomes negative, i.e. when the IR pulse arrives later than the visible pulse. The relative change of PL intensity does not vary much from *t* = -1 ps to -100 ps since the exciton lifetime of a QD is typically on the order of nanoseconds.

Phenomenologically, this IR-encoding mechanism differs significantly from mechanism 1 for dye molecules as it requires an opposite pulse sequence. The fact that the PL emission of molecular dyes is not subject to the electric field action of the IR pulse at negative delays could be due to that the molecular excitons are more spatially confined and molecular energy levels are more discretely distributed than those of QDs. In MD-WISE imaging, we take the advantage of the orthogonal behaviors of QDs and

molecular dyes to demonstrate the concept of distinguishing chromophores by solely varying the delay *t*. This concept has been indicated by the vertical red arrow in Fig. 1C.

Thus, up to now, we have presented two distinct mechanisms to encode PL with ultrashort mid-IR pulses, which enable three-dimensional multiplexing (time, IR and visible frequencies) of PL imaging – the foundation of MD-WISE imaging. Next, we will demonstrate the applications of both mechanisms.

***Distinguishing molecular dyes by tuning the IR frequency.***

We first demonstrate distinguishing two chromophores with nearly identical absorption and PL spectra using mid-IR vibrational excitations. The molecular dianion structures of fluorescein-5-isothiocyanate (FITC) and fluorescein are displayed in Fig. 4A, and they only differ by one functional group: the isothiocyanate (-N=C=S) group. As shown in Fig. 4B, the two molecules have nearly identical electronic absorption and emission spectra, making it difficult to distinguish them by choosing specific excitation or emission wavelengths. In contrast, MD-WISE microscopy should distinguish FITC from fluorescein by exciting the asymmetric stretch mode of the -N=C=S group. The DRIFTS results of FITC and fluorescein (Fig. 4C) show that they both have the generic xanthene ring stretch at 1600 $cm^{-1}$ (the green shade area) (44), and FITC has a unique isothiocyanate stretch mode at 2040 $cm^{-1}$ (the blue shade area) (45). The 2040 $cm^{-1}$ mode is accompanied by side bands that could be assigned to Fermi resonances between the -N=C=S stretch mode and the low frequency combination modes of the rings in FITC at ~1000 $cm^{-1}$ (45–47). Though the -N=C=S group is not directly attached to the xanthene rings, its stretch mode can affect PL intensity of the FITC dye, suggesting that the stretch mode could couple to the displacements of atoms in xanthene rings via Fermi resonances.

The effects of different vibrational modes on PL images are then investigated. The ultrafast kinetics of the PL intensity change of stained silica beads are plotted in Fig. 4D. When the IR frequency range is tuned to 1600 ± 30 $cm^{-1}$, both FITC and fluorescein show significant IR-induced PL intensity change over the delay time range of 0~10 ps. When the IR frequency range is tuned to 2040 ± 30 $cm^{-1}$, only FITC

shows PL intensity change. Comparing the percentage of PL change at fixed delays in the lower panel of Fig. 4D, the xanthene ring modes at 1600 $cm^{-1}$ have larger effects on the PL intensity than the -N=C=S stretch mode. This is expected because xanthene rings are directly responsible for the visible absorption and emission properties. However, the -N=C=S stretch mode encoding can be used to distinguish these two molecules.

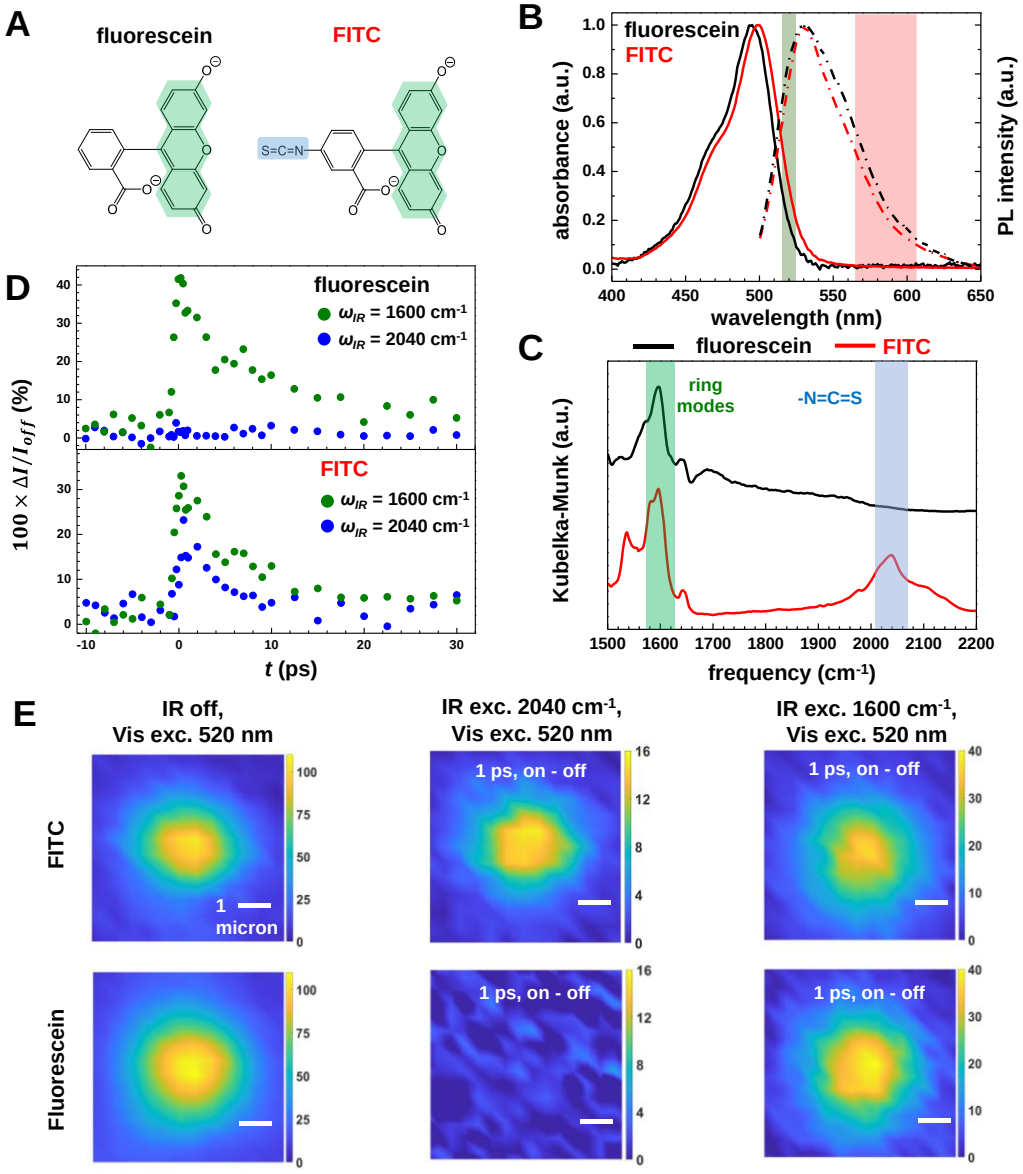


**Fig. 4 (A)** Molecular structures of fluorescein and FITC anions. The green shade area marks the aromatic rings responsible for fluorescence and the blue shade area marks the isothiocyanate group. **(B)** Steady-state absorption (solid lines) and emission (dashed lines) spectra of FITC and fluorescein adsorbed on silica beads. The green area marks (520 ± 5 nm) the excitation wavelength of the visible pulse, and red area (585 ± 18 nm) marks the collection window of fluorescence signals in MD-WISE imaging. **(C)** DRIFTS spectra of FITC and fluorescein. Tuning the IR center frequency to 1600 $cm^{-1}$ (green) or 2040 $cm^{-1}$ (blue) excites the common vibrational modes of the xanthene ring or the isothiocyanate group unique to FITC, respectively. **(D)** The ultrafast kinetic traces of the relative

difference of emission intensity in the widefield images induced by the IR pulse, measured using silica beads stained with FITC and fluorescein at 1600 $cm^{-1}$ and 2040 $cm^{-1}$. **(E)** The responses of stained beads at different conditions. Left column is the fluorescence image of a single 3-micron bead without IR pulse. The middle and right panels are the difference images at $t$ = +1 ps acquired at 1600 ± 30 $cm^{-1}$ and 2040 ± 30 $cm^{-1}$, respectively. All scale bars are 1 micron.

We now demonstrate differentiating FITC and fluorescence in microbeads by IR excitations in widefield MD-WISE images (Fig. 4E). The left column shows the PL images without applying the IR pulse. The middle and the right columns show the difference images acquired at short delay time of 1 ps using IR center frequencies of 1600 and 2040 $cm^{-1}$, respectively. Using 2040 $cm^{-1}$ IR excitation, it is evident that only the FITC-stained bead appears in the difference image while the fluorescein-stained bead is invisible. In contrast, the 1600 $cm^{-1}$ excitation makes beads dyed by both molecules visible. Thus, in addition to the example of the ester group in R6G molecule discussed above, the -N=C=S group on FITC marks another case where vibration of a functional group not attached to the xanthene rings can affect the PL emission. The results here demonstrate that dyes with nearly identical emission spectra can be used for multiplexing through their distinction in vibrational modes. The large IR absorption cross-section enables the IR-encoded PL images to be acquired in a widefield manner. Here, using relatively low pulse energies, 0.4 μJ of IR and 0.25 nJ of visible pulses, we can acquire images with a field of view of up to 20 microns without raster scanning.

***Distinguishing QDs from molecular dyes by tuning the ultrafast delay between pulses.***

The PL emission of QDs and molecules require opposite pulse sequences to encode the IR interactions. In MD-WISE imaging, we take advantage of the orthogonal behaviors of QDs and molecular dyes and demonstrate the concept of distinguishing chromophores by solely varying the delay $t$. In Fig. 5A, we show the PL images of mixed silica beads. The smaller 2-micron beads are stained with QDs and the larger 3-micron beads are stained with R6G molecules. We can capture both types of beads within the same view. The PL collection wavelength window covers the emission spectra of both QDs and R6G molecules. The IR frequency center is tuned to the 1600 $cm^{-1}$ xanthene ring mode of R6G, while there is no frequency requirement to encode the PL of QDs. At $t$ = -10 ps, the R6G-stained beads disappear from

the difference images in the bottom row of Fig. 5A, while QD-stained beads remain due to the significant quenching of PL intensity by the IR pulse. The orthogonal encoding behaviors of QDs and molecular dyes suggest that, for almost any emission color, we may choose a QD with a matching bandgap to act as the counterstain for the molecular dyes that emit the same color in PL imaging.

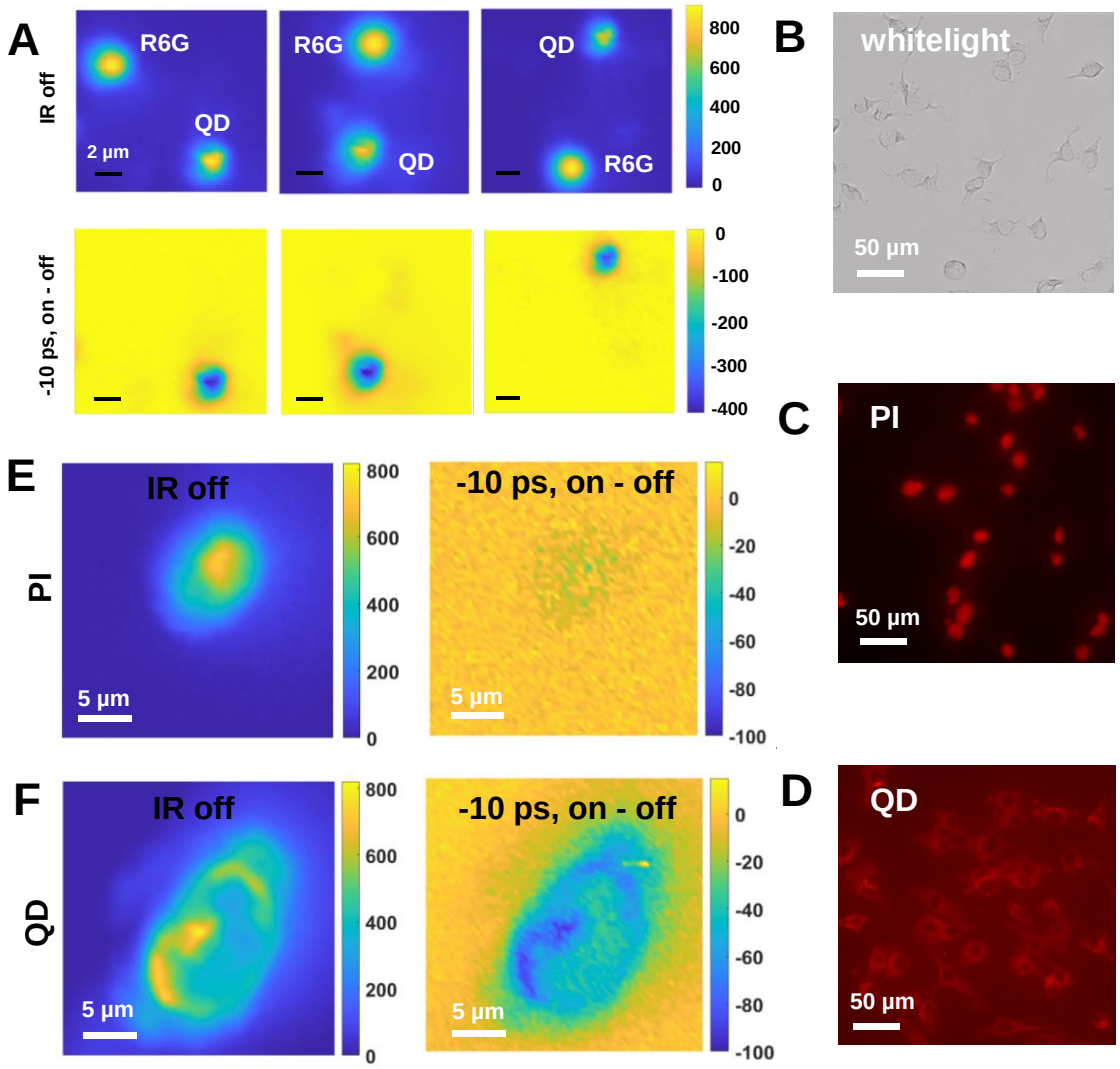


**Fig. 5 (A)** The top rows show three IR off images of 3-micron silica beads stained with R6G co-mixed with 2-micron silica beads stained with QDs. In the bottom row, the difference images acquired using an IR frequency centered at 1600 $cm^{-1}$ with delay set to -10 ps show that the QD beads can be distinguished from the R6G beads. The colorbars represent the counts on CCD pixels. Scale bars are 2 microns. **(B-D)** White light bright field image of fixed cells (B), and red-channel PL images of PI-stained (C) and QD-stained (D) fixed cells. **(E)** Widefield PL image of a PI-stained cell without using the IR pulse (left) and the difference PL image at -10 ps (right) acquired using MD-WISE microscopy. **(F)** Widefield PL image of a QD-stained cell without using the IR pulse (left) and the difference PL image at -10 ps (right) acquired using MD-WISE microscopy. All the images in panels E and F are acquired using IR frequency centered at 2100 $cm^{-1}$, visible excitation at 550 ± 5 nm and PL collection wavelength range of 585 ± 18 nm.

QD chromophores are bright PL emitters for biological imaging (48–50). We lastly demonstrate the proof-of-principle application of MD-WISE in differentiating QDs and molecule dyes in biological samples. The white light bright field images and conventional PL images of fixed human breast cancer cells are shown in Fig. 5 B-D. The cells are either stained by the QDs coated with streptavidin to visualize the cell membrane or the molecular dye propidium iodide (PI) to visualize the cell nucleus. Although the chromophores now are separated in the cells by their binding specificities to different biological structures, both the QD and the PI dye emit in the red channel of a conventional widefield PL microscope, and thus cannot be simply distinguished by PL emissions if we do not have the prior knowledge of the binding properties. To differentiate them, we applied the 2100 ± 30 $cm^{-1}$ IR excitation pulse following the visible pulse, and detect the change in PL emissions of both the QDs and the PI dyes. The IR frequency is chosen in the cell-silent IR region to avoid excess IR absorption by water and biomolecules in the cells. In Fig. 5E, although the regular PL image shows the cell nucleus, the difference image acquired at -10 ps only shows blank, indicating that there is no IR-induced PL change at this negative delay, verifying that the cell nucleus is stained by PI dyes. In Fig. 5F, the -10 ps difference image reproduces well the shape of the cell membrane as seen in the PL image acquired without the IR pulse, verifying that QDs coated with streptavidin only stain the cell membrane. The results demonstrate that the multiplexed MD-WISE microscopy can distinguish QD and molecular dyes as counterstains to each other by purely optical means even though these chromophores emit at the same detection channel.

**Concluding Remarks**

We have demonstrated here the concept of distinguishing chromophores in widefield PL imaging using independently tunable parameters such as the IR frequency and the ultrafast temporal delay in a three-dimensional multiplexed condition space. The orthogonal responses of chromophores to an ultrashort IR pulse shall not be limited to the demonstrated case here and can in principle be applied to distinguish other chromophores that have significantly overlapping emission spectra. Thus, highly multiplexed

imaging could become possible if many chromophores are created with proper designs for MD-WISE, building a library for simultaneous labeling and visualizing chemical species in complex systems (8, 51). To distinguish chromophores using different IR excitation frequencies, functional groups with distinct vibrational frequencies, such as isothiocyanate, nitrile, or azide groups, can be installed on bright fluorophores such as xanthene or cyanine dyes. Our works here show that there is much flexibility in the chemical sites where vibrational tags can be linked to fluorophores, simplifying the strategy and requirement to synthesize multiplexed palettes of fluorophores distinguishable by vibrational modes. To further expand the number of chromophores distinguishable by the temporal delay, one route is to find vibrational modes with lifetimes different enough that a significant portion of one chromophore remains in the vibrational excited state while the other chromophore has largely returned to the vibrational ground state (52).

Another new direction opened by this work is multiplexed widefield PL imaging without using exogeneous PL chromophore labels but using intrinsic PL such as the autofluorescence of the sample. Being able to image the intrinsic chemical species in a microscopic sample is central to our capacity of understanding and interacting with physical and biological systems. However, for instance, the autofluorescence of multiple species in biological samples often have overlapping emission spectra (53, 54). To enable multiplexed chemical PL imaging, MD-WISE method can either use the intrinsic vibrational modes of fluorescent biomolecules or the vibrational modes of modified molecules such as a tryptophan (55) tagged with a small, nonperturbative vibrational label.

The current MD-WISE microscopy was demonstrated using a conventional CCD without electron-multiplying (EM) capacity, and the visible excitation power is only ~0.25 nJ. Thus, there is a significant space for improvements in sensitivities, which can be straightforwardly achieved by more sensitive detectors and more powerful visible excitation lasers. For PL detection in the visible region, single particle or single molecule level sensitivity can nowadays be achieved routinely using an EM-CCD or avalanche photodiode detector (5, 15, 16, 33). Since the relative change of PL intensity induced by the IR

pulse can reach tens of percents at short delays and MD-WISE is based on the resonant excitation of the chromophore itself, the ultimate sensitivity limit of MD-WISE microscopy shall reach or become comparable to the single-molecule level when using highly sensitive detectors. This may in the future enable highly multiplexed super-resolution PL imaging. We also note that the relative PL intensity change in MD-WISE imaging is related to the field of view, since the photon flux of IR excitation is inversely proportional to the size of the illuminated area. Using an IR pulse energy of 1.5 microjoules, we can acquire images with a field of view of ~30 microns that contain a whole cell. Higher IR pulse energy can potentially enable >100 microns field of view and higher imaging speed in widefield imaging. Overall, the development of new PL probes and improvement of excitation and detection conditions for MD-WISE microscopy could enable highly sensitive multiplexed imaging and information acquisition on complex biological and chemical systems.

## Materials and Methods

**Materials.** R6G (catalog no. 83697), FITC (catalog no. F7250), fluorescein (catalog no. 46955), PI dyes (catalog no. P4170), and mesoporous silica microspheres (catalog no. 806587 for 2 micron, 806765 for 3 micron) were purchased from Sigma-Aldrich. Qdot™ 585 Streptavidin Conjugate (Invitrogen, catalog no. Q10111MP), EZ-Link™ Sulfo-NHS-SS-Biotin (catalog no. A39258) were purchased from Thermo Fisher. Ammine-coated CdSe/ZnS QD aqueous solutions were purchased from NN-Labs (catalog no. HECZWA560). All chemicals and materials were used without further purification.

**Staining of silica microbeads.** For the staining of silica microbeads with molecular dyes, dyes were diluted into ~1 mg/mL solutions (chloroform for R6G, ethanol for fluorescein and FITC), then the silica microbeads were soaked in the solutions and filtered. For fluorescein and FITC, 2 equivalent of NaOH (dissolved in ethanol) were added to form the bright dianions before adding the silica beads. For the staining using ammine-coated CdSe/ZnS QDs, QDs were diluted into 0.1 mg/mL aqueous solutions, then the silica microbeads were soaked in the solutions, then the water was removed by a rotary evaporator.

**Staining of fixed cells. 1. QD staining.** MDA-MB-231 human breast cancer cells (HTB-26) were obtained from American Type Culture Collection (ATCC; Manassas, VA) and cultured in Dulbecco's Modified Eagle's medium (Gibco; Waltham, MA) supplemented with 10% fetal bovine serum (Sigma-Aldrich; St. Louis, MO) at 37°C in a humidified incubator with 5% $CO_2$. The cells growing on coverslips at ~60% confluence were washed three times with phosphate-buffer saline (PBS) solutions at pH = 8.0. Then 250 µL PBS containing 0.5 mg/mL EZ-Link™ Sulfo-NHS-SS-Biotin was added. The cells were incubated at room temperature for 30 minutes, and then washed three times with ice-cold PBS. Cells were then fixed in 100% cold methanol for 10 min at -20°C, and then washed three times with PBS (5 min/wash). For the subsequent detection of biotin, we added 250 µL PBS containing 40 nM Qdot™ 585 Streptavidin Conjugate and incubated the cells for 1 hour at room temperature. The cells were then

washed three times with PBS and then rinsed with water. **2. PI staining.** The cells growing on coverslips at ~60% confluence were washed three times with PBS solutions at pH = 8.0. Cells were then fixed in 100% cold methanol for 10 min at -20°C, washed three times with PBS (5 min/wash), and then rinsed with 2× saline sodium citrate (SSC, containing 0.3 M NaCl, 0.03 M sodium citrate, pH 7.0) solution. Then, 250 µL of 500 µM PI dye aqueous solution was added to the cells for an incubation of 15 minutes. Cells were rinsed three times with 2X SSC and then with water. Bright field whitelight images and red-channel PL images are examined using a BZ-X710 microscope (TRITC red channel: excitation filter 540/25 nm, emission filter 605/70 nm, center/width).

**Linear optical measurements.** Diffuse reflectance infrared Fourier transform spectroscopy (DRIFTS) measurements were acquired on a Thermo Fisher Nicolet iS10 spectrometer by mixing the samples with KBr matrix. Linear UV/visible absorption spectra of stained beads were acquired on a Cary 60 spectrometer. Linear PL emission spectra of stained beads were acquired on a Hamamatsu Quantaurus-QY C11347 spectrometer. For UV/visible and PL measurements of the stained microbeads, the microbeads were sandwiched between two No.5 thin coverslips (Zeiss, 170 ± 5 microns) with transparent fluorolube oil to minimize scattering.

**Laser systems.** The femtosecond pulses used in the experiments here were produced using an Yb-based amplifier (Carbide, Light Conversion) pumping an optical parametric amplifier (Orpheus-One, Light Conversion) system. The repetition rate of the laser was set to 20 kHz. The mid-IR pulse was produced by the difference frequency generation crystal in the optical parametric amplifier, and the frequency center was tuned within the range of 1600~2100 $cm^{-1}$ depending on the need. The spectral full width at half maxima (FWHM) of the mid-IR output was ~60 $cm^{-1}$. For the non-biological samples, the mid-IR pulse energy was set to 0.4 microjoules using a pair of half-wave plate and polarizer. For the imaging of cells with a larger field of view (~30 microns), the mid-IR pulse energy used was 1.5 microjoules. The visible pulse for electronic excitation was generated by spectrally filtering a whitelight pulse, which was generated by focusing the optical parametric amplifier's 725 nm visible output into an yttrium aluminum garnet (YAG) crystal. For instance, the 550 ± 5 nm visible pulse was obtained by passing the whitelight pulse through a 550 ± 5 nm bandpass filter. The visible pulse energy after the filter was very low, estimated to be about only 0.25 nJ, equivalent to 5 microwatts at 20 kHz repetition rate. Thus, long exposure time of several seconds was used for the MD-WISE imaging experiments here, even for obtaining the IR-off plain PL images, but the exposure time shall not be an intrinsic limiting factor for the MD-WISE method. The duration of the IR and visible pulses were determined as < 300 femtoseconds by cross-correlation experiments. For the experiments below, the IR and visible pulses were combined collinearly using a customized dichroic mirror that reflects the visible pulse and transmits the IR pulse. The delay between the two pulses was controlled by a mechanized delay stage (Newport, XMS160).

**IR-pump whitelight-probe ultrafast transient absorption experiments.** R6G was dissolved in dimethyl sulfoxide-$d_6$ and the solution was sandwiched between two $CaF_2$ windows with a 56-micron spacer. The whitelight pulse and the mid-IR pulse were collinearly focused into the solution by a Schwarzchild reflective objective (Thorlabs, LMM40X-P01, numerical aperture 0.5). The beam size of both pulses at the focus was measured as 10~15 microns using a knife-edge method. The IR pulse was chopped by an optical chopper at 1 kHz. The whitelight pulse passing through the sample was collimated and attenuated before entering a spectrograph (300 l/mm grating, Shamrock 500i, Oxford Instruments) equipped with a conventional CCD detector (Newton 920, Oxford Instruments). The CCD's framerate was synchronized with the chopper at 1 kHz to collect the whitelight spectra when the IR pulse was blocked or unblocked, and the change of optical density induced by IR pulse, $\Delta A$, can be calculated at each wavelength. Transient absorption spectra were acquired at a series of temporal delays.

**MD-WISE imaging experiments.** The stained samples were placed on a No.5 thin coverslip (Zeiss, 170 ± 5 microns). The coverslip was mounted on a 2D piezo stage (MadCity Labs). The filtered visible pulse and the mid-IR pulse were focused onto the sample by a Schwarzchild reflective objective (PIKE Technologies Inc., PN 891-0001, numerical aperture 0.7). The field of view was adjustable, typically 10~20 microns for the imaging of silica microbeads and 30~40 microns for the imaging of fixed cells. The PL signals emitted by the chromophores passed through the coverslip and were collected by an infinity corrected 20X refractive objective (Zeiss, Fluar, numerical aperture 0.75). The PL signals then passed through a bandpass filter to remove the visible excitation pulse, and were projected directly on the Newton 920 CCD to form widefield images. The difference images in MD-WISE experiments were formed by subtracting the PL image collected when the IR beam was blocked by a mechanical shutter (IR off) from the PL image collected when the IR beam was unblocked (IR on). The CCD acquisition time was set to 0.5~10 seconds for each image collected with the IR beam on or off, depending on the brightness of the sample.

## Acknowledgements

The work is supported by National Institutes of Health, National Institute of General Medical Sciences, Grant 1R35GM138092-01(W.X.) and National Cancer Institute Grant R01CA266486 (S.E.W.). We thank Prof. Akif Tezcan, Yiying Li, and Qiufan Shi for providing help with sample preparation; Henry Agnew and Richa Rashmi from the Paesani group for helpful discussions on quantum chemical calculations for vibrational analysis. We thank Yuancheng Jing, Ricardo De-luna, and the MRSEC Materials Characterization Facility (MCF) at UC San Diego for providing help with linear PL measurements. We thank Prof. Wei Min for insightful discussions during manuscript preparation.

**Author contributions**: C.Y., and W.X. conceived and co-developed the concept of MD-WISE imaging. C.Y., J.C.W., C.W., J.R., Y.W. and S.E.W. performed experiments. C.Y., J.C.W., C.W., and J.R. performed staining on silica beads and collected the spectroscopic and imaging data. C.Y. analyzed the data. C.Y., J.C.W., and C.W. constructed the MD-WISE microscopy and related control software. S.E.W. and Y.W. performed staining on the fixed cells. C.L. performed quantum chemical calculations for vibrational analysis. C.Y. and W.X. wrote the manuscript, and all authors read and commented on the manuscript.

### References

1. W. E. Moerner, M. Orrit, Illuminating Single Molecules in Condensed Matter. *Science* **283**, 1670–1676 (1999).

2. S. Nie, D. T. Chiu, R. N. Zare, Probing Individual Molecules with Confocal Fluorescence Microscopy. *Science* **266**, 1018–1021 (1994).

3. S. W. Hell, J. Wichmann, Breaking the diffraction resolution limit by stimulated emission: stimulated-emission-depletion fluorescence microscopy. *Opt. Lett.* **19**, 780–782 (1994).

4. E. Betzig, *et al.*, Imaging Intracellular Fluorescent Proteins at Nanometer Resolution. *Science* **313**, 1642–1645 (2006).

5. M. J. Rust, M. Bates, X. Zhuang, Sub-diffraction-limit imaging by stochastic optical reconstruction microscopy (STORM). *Nat Methods* **3**, 793–796 (2006).

6. S. B. Penwell, L. D. S. Ginsberg, R. Noriega, N. S. Ginsberg, Resolving ultrafast exciton migration in organic solids at the nanoscale. *Nat Mater* **16**, 1136–1141 (2017).

7. J. R. Lakowicz, *Principles of Fluorescence Spectroscopy*, 3rd Ed. (Springer US, 2007).

8. L. Wei, *et al.*, Super-multiplex vibrational imaging. *Nature* **544**, 465–470 (2017).

9. C. W. Freudiger, *et al.*, Label-Free Biomedical Imaging with High Sensitivity by Stimulated Raman Scattering Microscopy. *Science* **322**, 1857–1861 (2008).

10. A. Zumbusch, G. R. Holtom, X. S. Xie, Three-Dimensional Vibrational Imaging by Coherent Anti-Stokes Raman Scattering. *Phys Rev Lett* **82**, 4142–4145 (1999).

11. Y. Bai, *et al.*, Ultrafast chemical imaging by widefield photothermal sensing of infrared absorption. *Sci Adv* **5**, eaav7127 (2023).

12. J. C. Wright, Double Resonance Excitation of Fluorescence in the Condensed Phase—An Alternative to Infrared, Raman, and Fluorescence Spectroscopy. *Appl. Spectrosc.* **34**, 151–157 (1980).

13. A. Seilmeier, W. Kaiser, A. Laubereau, S. F. Fischer, A novel spectroscopy using ultrafast two-pulse excitation of large polyatomic molecules. *Chem Phys Lett* **58**, 225–229 (1978).

14. T. Ohmori, M. Sakai, M. Ishihara, M. Kikuchi, M. Fujii, Cell imaging by transient fluorescence detected infrared microscopy in *Proc.SPIE*, (2008), p. 685307.

15. H. Xiong, *et al.*, Stimulated Raman excited fluorescence spectroscopy and imaging. *Nat Photonics* **13**, 412–417 (2019).

16. L. Whaley-Mayda, A. Guha, S. B. Penwell, A. Tokmakoff, Fluorescence-Encoded Infrared Vibrational Spectroscopy with Single-Molecule Sensitivity. *J Am Chem Soc* **143**, 3060–3064 (2021).

17. Y. Zhang, *et al.*, Fluorescence-Detected Mid-Infrared Photothermal Microscopy. *J Am Chem Soc* **143**, 11490–11499 (2021).

18. M. Li, *et al.*, Fluorescence-Detected Mid-Infrared Photothermal Microscopy. *J Am Chem Soc* **143**, 10809–10815 (2021).

19. H. Xiong, *et al.*, Super-resolution vibrational microscopy by stimulated Raman excited fluorescence. *Light Sci Appl* **10**, 87 (2021).

20. A. Gaiduk, P. v Ruijgrok, M. Yorulmaz, M. Orrit, Detection limits in photothermal microscopy. *Chem Sci* **1**, 343–350 (2010).

21. A. Gaiduk, M. Yorulmaz, P. V Ruijgrok, M. Orrit, Room-Temperature Detection of a Single Molecule's Absorption by Photothermal Contrast. *Science* **330**, 353–356 (2010).

22. A. Mau, K. Friedl, C. Leterrier, N. Bourg, S. Lévêque-Fort, Fast widefield scan provides tunable and uniform illumination optimizing super-resolution microscopy on large fields. *Nat Commun* **12**, 3077 (2021).

23. Y. Guo, *et al.*, Visualizing Intracellular Organelle and Cytoskeletal Interactions at Nanoscale Resolution on Millisecond Timescales. *Cell* **175**, 1430-1442.e17 (2018).

24. M. Delor, H. L. Weaver, Q. Yu, N. S. Ginsberg, Imaging material functionality through three-dimensional nanoscale tracking of energy flow. *Nat Mater* **19**, 56–62 (2020).

25. K. (石井邦彦) Ishii, S. (竹内佐年) Takeuchi, T. (田原太平) Tahara, Infrared-induced coherent vibration of a hydrogen-bonded system: Effects of mechanical and electrical anharmonic couplings. *J Chem Phys* **131**, 044512 (2009).

26. E. A. Arsenault, P. Bhattacharyya, Y. Yoneda, G. R. Fleming, Two-dimensional electronic–vibrational spectroscopy: Exploring the interplay of electrons and nuclei in excited state molecular dynamics. *J Chem Phys* **155**, 020901 (2021).

27. L. J. G. W. van Wilderen, A. T. Messmer, J. Bredenbeck, Mixed IR/Vis Two-Dimensional Spectroscopy: Chemical Exchange beyond the Vibrational Lifetime and Sub-ensemble Selective Photochemistry. *Angew Chem Int Ed* **53**, 2667–2672 (2014).

28. M. Sakai, Y. Kawashima, A. Takeda, T. Ohmori, M. Fujii, Far-field infrared super-resolution microscopy using picosecond time-resolved transient fluorescence detected IR spectroscopy. *Chem Phys Lett* **439**, 171–176 (2007).

29. N. Bokor, K. Inoue, S. Kogure, M. Fujii, M. Sakai, Visible-super-resolution infrared microscopy using saturated transient fluorescence detected infrared spectroscopy. *Opt Commun* **283**, 509–514 (2010).

30. K. Inoue, N. Bokor, S. Kogure, M. Fujii, M. Sakai, Two-point-separation in a sub-micron nonscanning IR super-resolution microscope based on transient fluorescence detected IR spectroscopy. *Opt Express* **17**, 12013–12018 (2009).

31. J. Hebling, K.-L. Yeh, M. C. Hoffmann, B. Bartal, K. A. Nelson, Generation of high-power terahertz pulses by tilted-pulse-front excitation and their application possibilities. *J Opt Soc Am B* **25**, B6–B19 (2008).

32. C. Manzoni, M. Först, H. Ehrke, A. Cavalleri, Single-shot detection and direct control of carrier phase drift of midinfrared pulses. *Opt Lett* **35**, 757–759 (2010).

33. J. Shi, *et al.*, All-optical fluorescence blinking control in quantum dots with ultrafast mid-infrared pulses. *Nat Nanotechnol* **16**, 1355–1361 (2021).

34. J. N. Mastron, A. Tokmakoff, Fourier Transform Fluorescence-Encoded Infrared Spectroscopy. *J Phys Chem A* **122**, 554–562 (2018).

35. L. Whaley-Mayda, A. Guha, A. Tokmakoff, Resonance conditions, detection quality, and single-molecule sensitivity in fluorescence-encoded infrared vibrational spectroscopy. *J Chem Phys* **156**, 174202 (2022).

36. L. Whaley-Mayda, S. B. Penwell, A. Tokmakoff, Fluorescence-Encoded Infrared Spectroscopy: Ultrafast Vibrational Spectroscopy on Small Ensembles of Molecules in Solution. *J Phys Chem Lett* **10**, 1967–1972 (2019).

37. G. S. S. Saini, *et al.*, Rhodamine 6G interaction with solvents studied by vibrational spectroscopy and density functional theory. *J Mol Struct* **931**, 10–19 (2009).

38. H. Watanabe, N. Hayazawa, Y. Inouye, S. Kawata, DFT Vibrational Calculations of Rhodamine 6G Adsorbed on Silver: Analysis of Tip-Enhanced Raman Spectroscopy. *J Phys Chem B* **109**, 5012–5020 (2005).

39. M. Kasha, Characterization of electronic transitions in complex molecules. *Discuss Faraday Soc* **9**, 14–19 (1950).

40. K. Tarafder, Y. Surendranath, J. H. Olshansky, A. P. Alivisatos, L.-W. Wang, Hole Transfer Dynamics from a CdSe/CdS Quantum Rod to a Tethered Ferrocene Derivative. *J Am Chem Soc* **136**, 5121–5131 (2014).

41. O. M. Pearce, J. S. Duncan, N. H. Damrauer, G. Dukovic, Ultrafast Hole Transfer from CdS Quantum Dots to a Water Oxidation Catalyst. *J Phys Chem C* **122**, 17559–17565 (2018).

42. M. Y. Ivanov, M. Spanner, O. Smirnova, Anatomy of strong field ionization. *J Mod Opt* **52**, 165–184 (2005).

43. S. V Popruzhenko, Keldysh theory of strong field ionization: history, applications, difficulties and perspectives. *J Phys B-At Mol Opt* **47**, 204001 (2014).

44. T. Maeda, T. Nagahara, M. Aida, T. Ishibashi, Identification of chemical species of fluorescein isothiocyanate isomer-I (FITC) monolayers on platinum by doubly resonant sum-frequency generation spectroscopy. *J Raman Spectrosc* **39**, 1694–1702 (2008).

45. J. Yenagi, A. R. Nandurkar, J. Tonannavar, 2-Methoxyphenyl isocyanate and 2-Methoxyphenyl isothiocyanate: Conformers, vibration structure and multiplet Fermi resonance. *Spectrochim Acta A Mol Biomol Spectrosc* **91**, 261–268 (2012).

46. J. Y. Park, *et al.*, Effect of isotope substitution on the Fermi resonance and vibrational lifetime of unnatural amino acids modified with IR probe: A 2D-IR and pump-probe study of 4-azido-L-phenyl alanine. *J Chem Phys* **153**, 164309 (2020).

47. J. Zhang, *et al.*, Identifying and Modulating Accidental Fermi Resonance: 2D IR and DFT Study of 4-Azido-l-phenylalanine. *J Phys Chem B* **122**, 8122–8133 (2018).

48. W. Liu, *et al.*, Compact Biocompatible Quantum Dots Functionalized for Cellular Imaging. *J Am Chem Soc* **130**, 1274–1284 (2008).

49. J. K. Jaiswal, E. R. Goldman, H. Mattoussi, S. M. Simon, Use of quantum dots for live cell imaging. *Nat Methods* **1**, 73–78 (2004).

50. M. Bruchez, M. Moronne, P. Gin, S. Weiss, A. P. Alivisatos, Semiconductor Nanocrystals as Fluorescent Biological Labels. *Science* **281**, 2013–2016 (1998).

51. F.-K. Lu, *et al.*, Label-free DNA imaging in vivo with stimulated Raman scattering microscopy. *Proc Natl Acad Sci USA* **112**, 11624–11629 (2015).

52. S. M. Fica-Contreras, *et al.*, Long Vibrational Lifetime R-Selenocyanate Probes for Ultrafast Infrared Spectroscopy: Properties and Synthesis. *J Phys Chem B* **125**, 8907–8918 (2021).

53. W. R. Zipfel, *et al.*, Live tissue intrinsic emission microscopy using multiphoton-excited native fluorescence and second harmonic generation. *Proc Natl Acad Sci USA* **100**, 7075–7080 (2003).

54. I. Georgakoudi, *et al.*, NAD(P)H and Collagen as in Vivo Quantitative Fluorescent Biomarkers of Epithelial Precancerous Changes1. *Cancer Res* **62**, 682–687 (2002).

55. D. Zhong, S. K. Pal, D. Zhang, S. I. Chan, A. H. Zewail, Femtosecond dynamics of rubredoxin: Tryptophan solvation and resonance energy transfer in the protein. *Proc Natl Acad Sci USA* **99**, 13–18 (2002).